https://doi.org/10.20965/jdr.2019.p0225

Paper:

Development and Applicability of Multiscale Multiphysics Integrated Simulator for Tsunami

Taro Arikawa*,†, Yu Chida, Katsumi Seki*, Tomohiro Takagawa**, and Kenichiro Shimosako****

*Chuo University
1-13-27 Kasuga, Bunkyo, Tokyo 112-8551, Japan
†Corresponding author, E-mail: taro.arikawa.38d@g.chuo-u.ac.jp
**Port and Airport Research Institute, Kanagawa, Japan
[Received January 20, 2019; accepted February 12, 2019]

In this research, we develop a numerical fluid simulator coupled with a structural analysis. The purpose of this system is to efficiently calculate all stages of a tsunami from source to runup, including structural deformation. We also investigate the stability of breakwaters at Kamaishi port. The numerical results are compared with physical experiments, revealing good agreement. The system is applied to the local conditions at Kamaishi port to verify its applicability. Most of the breakwaters are washed away, which is similar to the actual reported damage, indicating that the proposed system can effectively reproduce tsunami structural damage.

Keywords: real-time tsunami forecast, tsunami inundation, ocean bottom observation network, tsunami disaster response

1. Introduction

To accurately predict and evaluate inundation damage caused by very large tsunamis, it is necessary to accurately calculate not only the overflow from defensive structures such as breakwaters and seawalls but also the breakage condition due to destruction of the structures. In order to accurately calculate tsunami propagation, it is important to simulate a large area from the wave source of the earthquake to the land. Moreover, to analyze the structural deformation with high accuracy, surrounding topography and structural information is required. However, current computer capacities make these calculations difficult. Therefore, multiscale and multiphysics simulation systems are key tools for accurate predictions of tsunami inundation damage.

However, no method has yet been developed that can simulate tsunami waves from source to inundation along with structural deformation. Therefore, in this study, we developed a method to hierarchically combine various simulators and calculate tsunami occurrence, propagation, inundation, and destruction of structures. We then verify the validity of this method.

2. Methodology

2.1. Overview of the System

In this research, we constructed a numerical system that combines five different simulations in order to perform a series of calculations from the wave source of a tsunami up to the destruction of structures (**Fig. 1**). First, from tsunami occurrence to propagation, we used a multilayered nonlinear long wave equation assuming hydrostatic pressure (STOC-ML [1]). It connects single-phase Navier–Stokes (NS) equations (CADMAS-SURF/3D [2]) that calculate the sea surface using the VOF (volume of fluid) method; however, we also inserted a single-phase NS equation that calculates the sea surface using a continuity equation (STOC-IC [1]) to act as a buffer. Furthermore, to account for the influence of the gas phase, a single-phase VOF method and a gas-liquid two-phase VOF method (CADMAS-2F [3]) were connected. Finally, a structure-foundation simulator (STR [4]) was added, which is calculated by FEM.

2.2. Governing Equations of Each Simulator

2.2.1. STOC-ML

The basic equations are a continuity equation (Eq. (1)), an x direction motion equation (Eq. (2)), a y direction motion equation (Eq. (3)), and a hydrostatic equation (Eq. (4)) described in the Cartesian coordinate system. The free surface equation (Eq. (5)) and the z direction flow velocity are determined from the continuity equation.

$$\frac{\partial}{\partial x}(\gamma_x u)+\frac{\partial}{\partial y}(\gamma_y v)+\frac{\partial}{\partial z}(\gamma_z w)=0 \quad \ldots\ldots \quad (1)$$

$$\begin{aligned}\gamma_v\frac{\partial u}{\partial t}&+\frac{\partial}{\partial x}(\gamma_x uu)+\frac{\partial}{\partial y}(\gamma_y vu)+\frac{\partial}{\partial z}(\gamma_z wu)-f_0 v\\ =&\ -\gamma_v\frac{1}{\rho_0}\frac{\partial p}{\partial x}+\frac{\partial}{\partial x}\left(\gamma_x \nu_H 2\frac{\partial u}{\partial x}\right)\\ &+\frac{\partial}{\partial y}\left\{\gamma_y \nu_H\left(\frac{\partial u}{\partial y}+\frac{\partial v}{\partial x}\right)\right\}\\ &+\frac{\partial}{\partial z}\left\{\gamma_z \nu_V\left(\frac{\partial u}{\partial z}+\frac{\partial w}{\partial x}\right)\right\} \quad \ldots\ldots \quad (2)\end{aligned}$$

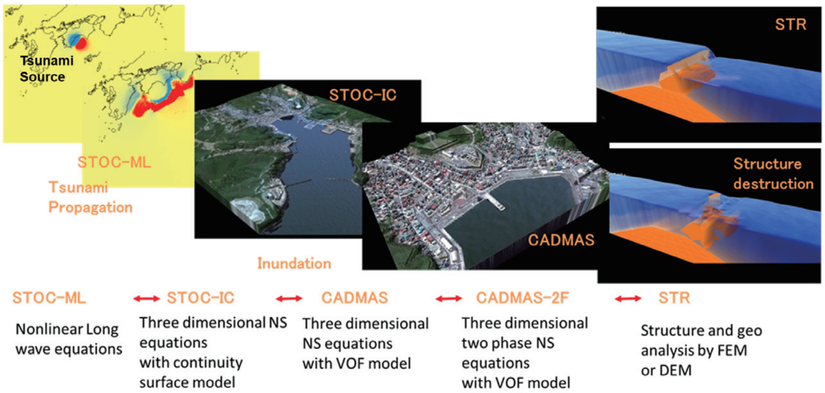

Fig. 1. Multiscale Multiphysics Integrated Calculator for Storm surge and Tsunami (MMICST).

$$\begin{aligned}
&\gamma_v \frac{\partial v}{\partial t} + \frac{\partial}{\partial x}(\gamma_x uv) + \frac{\partial}{\partial y}(\gamma_y vv) + \frac{\partial}{\partial z}(\gamma_z wv) + f_0 u \\
&= -\gamma_v \frac{1}{\rho_0}\frac{\partial p}{\partial y} + \frac{\partial}{\partial x}\left\{\gamma_x \nu_H \left(\frac{\partial v}{\partial x} + \frac{\partial u}{\partial y}\right)\right\} \\
&\quad + \frac{\partial}{\partial y}\left(\gamma_y \nu_H 2 \frac{\partial v}{\partial y}\right) \\
&\quad + \frac{\partial}{\partial z}\left\{\gamma_z \nu_V \left(\frac{\partial v}{\partial z} + \frac{\partial w}{\partial y}\right)\right\} \quad \ldots\ldots \quad (3)
\end{aligned}$$

$$0 = -\frac{1}{\rho_0}\frac{\partial p}{\partial z} + g \quad \ldots\ldots\ldots\ldots \quad (4)$$

$$\gamma_z \frac{\partial \eta}{\partial t} + \frac{\partial}{\partial x}\int_{-h}^{\eta} \gamma_x u dz + \frac{\partial}{\partial y}\int_{-h}^{\eta} \gamma_y v dz = 0 \quad \ldots \quad (5)$$

Here, x, y, z are the coordinates in the axial direction of the Cartesian coordinate system, u, v, w are the flow velocities in the x, y, z axis directions, η is the water level, h is the water depth from the reference water surface, ρ is the density, p is the pressure, γ_v is the effective volume porosity (the volume ratio of the liquid phase of the mesh: $0.0 \leqq \gamma_v \leqq 1.0$), γ_x, γ_y, γ_z are the effective areal porosity in the x, y, z direction (areal ratio of liquid phase: $0.0 \leqq \gamma_x, \gamma_y, \gamma_z \leqq 1.0$), g is the gravitational acceleration, ν_H is the kinematic viscosity in the horizontal direction, and ν_v is the kinematic viscosity coefficient in the vertical direction. f_0 is the Coriolis parameter.

2.2.2. STOC-IC

STOC-IC is a non-hydrostatic pressure model. Instead of Eq. (4), the NS equation (Eq. (6)) is used in the vertical direction.

$$\begin{aligned}
&\gamma_v \frac{\partial w}{\partial t} + \frac{\partial}{\partial x}(\gamma_x uw) + \frac{\partial}{\partial y}(\gamma_y vw) + \frac{\partial}{\partial z}(\gamma_z ww) \\
&= -\gamma_v \frac{1}{\rho_0}\frac{\partial p}{\partial z} + \gamma_v g + \frac{\partial}{\partial x}\left\{\gamma_x \nu_H \left(\frac{\partial w}{\partial x} + \frac{\partial u}{\partial z}\right)\right\} \\
&\quad + \frac{\partial}{\partial y}\left\{\gamma_y \nu_H \left(\frac{\partial w}{\partial y} + \frac{\partial v}{\partial z}\right)\right\} + \frac{\partial}{\partial z}\left(\gamma_z \nu_V 2 \frac{\partial w}{\partial z}\right) \\
&\quad \ldots\ldots\ldots\ldots\ldots \quad (6)
\end{aligned}$$

2.2.3. CADMAS-SURF/3D and CADMAS-2F

CADMAS-SURF/3D uses a continuity equation and NS equations for a three-dimensional incompressible viscous fluid based on a porous model as the basic equations (Eqs. (7)–(10)). For the free surface analysis model, we used the VOF method, which can analyze complex surface shapes (Eq. (11)). In the gas-liquid two-phase model (CADMAS-2F), the gas phase density (ρ_G) was calculated. It has a temporal and spatial distribution due to the introduction of compressibility and $\dot{\rho}_G$ follows Eq. (12), which is a substantial derivative of the gas phase density.

$$\frac{\partial \gamma_x u}{\partial x} + \frac{\partial \gamma_y v}{\partial y} + \frac{\partial \gamma_z w}{\partial z} = \gamma_v S_\rho - \frac{1-F}{\rho_G}\dot{\rho}_G \quad \ldots \quad (7)$$

$$\begin{aligned}
&\lambda_v \frac{\partial u}{\partial t} + \frac{\partial \lambda_x uu}{\partial x} + \frac{\partial \lambda_y vu}{\partial y} + \frac{\partial \lambda_z wu}{\partial z} \\
&= -\frac{\gamma_v}{\rho}\frac{\partial p}{\partial x} - u\frac{1-F}{\rho_G}\dot{\rho}_G + \frac{\partial}{\partial x}\left\{\gamma_x \nu_e \left(2\frac{\partial u}{\partial x}\right)\right\} \\
&\quad + \frac{\partial}{\partial y}\left\{\gamma_y \nu_e \left(\frac{\partial u}{\partial y} + \frac{\partial v}{\partial x}\right)\right\} \\
&\quad + \frac{\partial}{\partial z}\left\{\gamma_z \nu_e \left(\frac{\partial u}{\partial z} + \frac{\partial w}{\partial x}\right)\right\} \\
&\quad - \gamma_v D_x u - R_x + \gamma_v S_u \quad \ldots\ldots\ldots \quad (8)
\end{aligned}$$

$$\begin{aligned}
&\lambda_v \frac{\partial v}{\partial t} + \frac{\partial \lambda_x uv}{\partial x} + \frac{\partial \lambda_y vv}{\partial y} + \frac{\partial \lambda_z wv}{\partial z} \\
&= -\frac{\gamma_v}{\rho}\frac{\partial p}{\partial y} - v\frac{1-F}{\rho_G}\dot{\rho}_G \\
&\quad + \frac{\partial}{\partial x}\left\{\gamma_x \nu_e \left(\frac{\partial v}{\partial x} + \frac{\partial u}{\partial y}\right)\right\} \\
&\quad + \frac{\partial}{\partial y}\left\{\gamma_y \nu_e \left(2\frac{\partial v}{\partial y}\right)\right\} \\
&\quad + \frac{\partial}{\partial z}\left\{\gamma_z \nu_e \left(\frac{\partial v}{\partial z} + \frac{\partial w}{\partial y}\right)\right\} \\
&\quad - \gamma_v D_y v - R_y + \gamma_v S_v \quad \ldots\ldots\ldots \quad (9)
\end{aligned}$$

$$\begin{aligned}
&\lambda_v \frac{\partial w}{\partial t} + \frac{\partial \lambda_x uw}{\partial x} + \frac{\partial \lambda_y vw}{\partial y} + \frac{\partial \lambda_z ww}{\partial z} \\
&= \quad -\frac{\gamma_v}{\rho}\frac{\partial p}{\partial z} - w\frac{1-F}{\rho_G}\dot{\rho}_G \\
&\qquad + \frac{\partial}{\partial x}\left\{\gamma_x \nu_e \left(\frac{\partial w}{\partial x} + \frac{\partial u}{\partial z}\right)\right\} \\
&\qquad + \frac{\partial}{\partial y}\left\{\gamma_y \nu_e \left(\frac{\partial w}{\partial y} + \frac{\partial v}{\partial z}\right)\right\} \\
&\qquad + \frac{\partial}{\partial z}\left\{\gamma_z \nu_e \left(2\frac{\partial w}{\partial z}\right)\right\} \\
&\qquad - \gamma_v D_z w - R_z + \gamma_v S_w - \frac{\gamma_v \rho^* g}{\rho} \quad \dots\dots \quad (10)
\end{aligned}$$

$$\gamma_v \frac{\partial F}{\partial t} + \frac{\partial \gamma_x uF}{\partial x} + \frac{\partial \gamma_y vF}{\partial y} + \frac{\partial \gamma_z wF}{\partial z} = \gamma_v S_F \quad (11)$$

$$\dot{\rho}_G = \gamma_v \frac{\partial \rho_G}{\partial t} + \gamma_x u\frac{\partial \rho_G}{\partial x} + \gamma_y v\frac{\partial \rho_G}{\partial y} + \gamma_z w\frac{\partial \rho_G}{\partial z} \quad (12)$$

Here, F is the volume of fluid. S_F is the source term for wave generation, $\rho*$ is the density considering buoyancy, p is the pressure, ν_e is the sum of kinetic viscosity (ν) and eddy viscosity (ν_t), and λ_v, λ_x, λ_y, λ_z is expressed as Eq. (13) with C_M as the inertial force coefficient.

$$\left.\begin{aligned}
\lambda_v &= \gamma_v + (1-\gamma_v)C_M \\
\lambda_x &= \gamma_x + (1-\gamma_x)C_M \\
\lambda_y &= \gamma_y + (1-\gamma_y)C_M \\
\lambda_z &= \gamma_z + (1-\gamma_z)C_M
\end{aligned}\right\} \quad \dots\dots\dots \quad (13)$$

Also, D_x, D_y, D_z are coefficients for the energy dissipating zone, S_ρ, S_u, S_v, S_w are source terms for wave generation, and the resistance forces from the porous body (R_x, R_y, R_z) are modeled in a form proportional to the square of the flow velocity (Eq. (14)), with C_D as the resistance force coefficient.

$$\left.\begin{aligned}
R_x &= \frac{1}{2}\frac{C_D}{\Delta x}(1-\gamma_x)\,u\sqrt{u^2+v^2+w^2} \\
R_y &= \frac{1}{2}\frac{C_D}{\Delta y}(1-\gamma_y)\,v\sqrt{u^2+v^2+w^2} \\
R_z &= \frac{1}{2}\frac{C_D}{\Delta z}(1-\gamma_z)\,w\sqrt{u^2+v^2+w^2}
\end{aligned}\right\} \quad \dots \quad (14)$$

where Δ_x, Δ_x, Δ_x are the grid sizes in the x, y, z direction.

2.2.4. STR

STR calculates deformation of structures and the ground. STR receives pressure from the fluid side and sends the deformation volume to the fluid side. The governing equation is expressed by Eq. (15):

$$\rho_s \frac{\partial^2 u_{si}}{\partial t^2} = \sigma_{ij,j} + \rho_s \ddot{a} \quad \dots\dots\dots\dots \quad (15)$$

where σ_{ij} is the stress tensor, ρ_s is the density, $\ddot{a}$ is the acceleration of the external force, and u_s is the displacement. For the ground, calculations are performed using Eqs. (16) and (17):

$$\rho \frac{\partial^2 u_{si}}{\partial t^2} = \sigma_{ij,j} + \rho g \quad \dots\dots\dots\dots \quad (16)$$

$$\sigma'_{ij} = \sigma_{ij} + p' I_{ij} \quad \dots\dots\dots\dots \quad (17)$$

where ρ is the density of the ground, calculated by Eq. (18), σ'_{ij} is the effective stress tensor, p' is the pore water pressure, and I_{ij} is the unit tensor.

$$\rho = (1-n)\rho_s + n\rho_f \quad \dots\dots\dots\dots \quad (18)$$

Here, n is the porosity, ρ_s is the density of the soil particles, and ρ_f is the density of the pore water.

A seepage analysis of the ground was also performed. The equation of motion and the mass conservation formula are as follows.

$$\begin{aligned}
\dot{\boldsymbol{w}} &= k\left(-\nabla p + \rho_f \boldsymbol{g} - \rho_f \ddot{\boldsymbol{u}}\right) \quad \dots\dots \quad (19) \\
\nabla \cdot \dot{\boldsymbol{w}} &= -\nabla \cdot \dot{\boldsymbol{u}} - C_{Kf}\dot{p} \quad \dots\dots\dots \quad (20)
\end{aligned}$$

where w is the relative displacement of the pore water to the ground, k is the permeability coefficient, and $C_{kf} = n/K_f$ and K_f is the bulk modulus of the pore water.

2.3. Coupling Method

All connections are made using the MPI library. The coupling method of STOC-ML and STOC-IC has previously been described in [1]. In addition, the coupling methods of STOC-IC and CADMAS and CAMAS-2F and STR have been described in detail in [5] and [4] respectively. The same method was used for the coupling of CADMAS-SURF/3D and CADMAS-2F as for STOC-IC and CADMAS-SURF/3D.

2.4. Measures Against Abnormal Pressure in CADMAS-2F Due to Structural Movement

When the structure moves, a problem arises in CADMAS-2F whereby the pressure increases when the gap between the structure and the fluid cell becomes too small.

2.4.1. Mechanism of Abnormal Pressure

1) Problem of gap velocity

By repeating steps (a)–(c) below, abnormal pressure is generated.

(a) Velocity (v_A) is used to calculate the z direction momentum entering through the interface of the control volume. (b) When passing through the interface, v_A should be decelerated due to expansion of the flow area, but because v_A is used in CADMAS, the temporary velocity becomes too large to solve the matrix solver. (c) When correcting the temporary velocity using the pressure gradient to satisfy mass conservation, a large pressure gradient occurs between cells No.1 and No.2 (cell No.1 pressure > cell No.2 pressure). The above cycle is repeated, the distance between the structure and the x direction grid line decreases, and the pressure of cell No.1 rises, resulting in an abnormal value (**Fig. 2**).

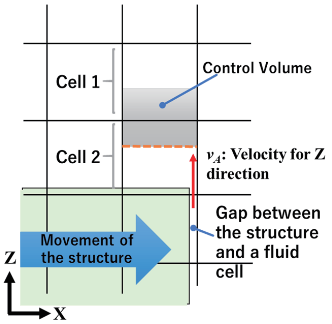

Fig. 2. Mechanism of abnormal pressure (1).

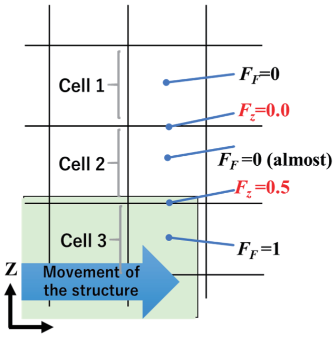

Fig. 3. Mechanism of abnormal pressure (2).

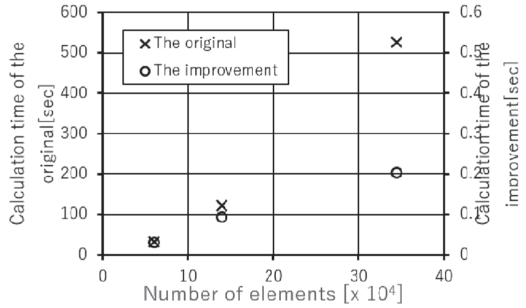

Fig. 4. Difference in calculation time due to surface element extraction processing.

2) Sudden change in density at the surface

In addition, a pressure abnormality is also caused by a sudden change in density at the surface (**Fig. 3**). Using the F_F (VOF function value) and F_Z (VOF function value of z interface) value of each cell, the density at the interface is calculated by the following equation;

$$\rho' = \rho_w F_z + \rho_a (1 - F_z) \quad \quad (21)$$

where ρ' is the density at the interface, ρ_w is the density of water, and ρ_a is the density of air. $1/\rho$ is applied to the pressure gradient term when calculating the equation of motion. As the density of water and the density of air differ by an order of 10^3, to correct the same momentum, the pressure gradient between cell No.1 and cell No.2 must be several hundred times the pressure gradient between cell No.2 and cell No.3.

3) Measures

Therefore, with respect to the gap velocity, the velocity used as the z direction momentum entering the control volume No.1 through the interface should be kept below the value of the flow rate (areal porosity); i.e.:

$$v_A' = \frac{\gamma_{vB}}{\gamma_{vA}} v_A \quad \quad (22)$$

where v_A' is the flow velocity after the change, γ_{vB} is the z direction areal porosity at the interface between the structure and the x direction grid lines, and γ_{vA} is the z direction areal porosity at the interface.

For the problem of the sudden change of density, the lower limit of F_z between cell No.2 and cell No.3 was set to 0.1. This reduced the imbalance in density that led to imbalance in the pressure gradient.

2.5. Extracting Outer Surface Elements of the Structure

In the coupled calculation of CADMAS and STR, the outer surface elements of the structure were extracted, and the pressure received by the structure was calculated. The surfaces that compose each element were then collated; if no matches were found, it was extracted as a surface element. When searching, it takes time to process if the constituent faces of all elements are targeted. Therefore, the search candidates were reduced to speed up the processing.

First, before each search, data on all surfaces whose node is the first constituent node was held for each node. Next, when searching for a surface that coincides with the target surface, we set one surface data point of the target node as a search candidate on the surface, which was regarded as the first constituent node. As a result, the calculation speed was improved by approximately 1500 times (**Fig. 4**).

3. Validity of the Proposed System

3.1. Comparison with Experimental Data

To verify the numerical model, the simulated destruction of breakwaters due to overflow was compared with that determined by physical experiments [6]. **Fig. 5** shows the cross-section of the numerical calculation, where the grid size of x, y, and z was 0.010 m each. The detail information about cross section was same as the physical experiments. Young's modulus was 2.35×10^{11}, Poisson's ratio was 0.333, the density of the caisson was 2349 kg/m^3, the density of the rubble mound was 2135 kg/m^3, the static friction coefficient was 0.6, and the dynamic friction was 0.2.

3.2. Results

Figure 6 shows a comparison between calculated and experimental caisson movement, which are qualitatively

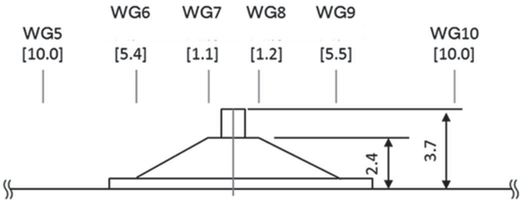

Fig. 5. Cross section of numerical simulations.

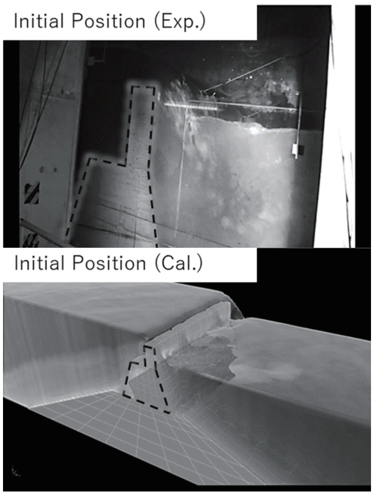

(a) Initial position

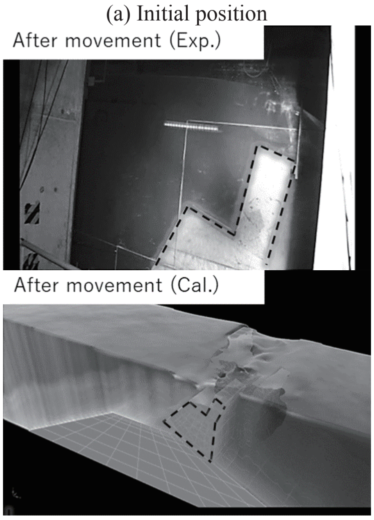

(b) After movement

Fig. 6. Comparison of caisson movement between experiments and calculations.

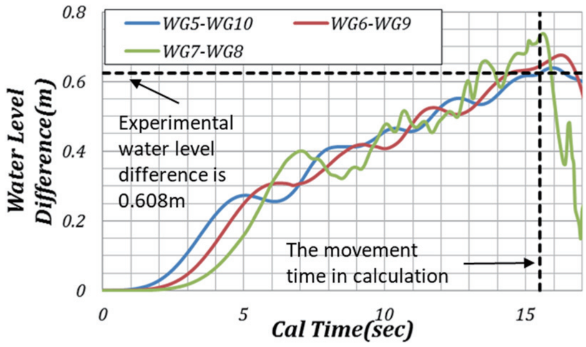

Fig. 7. Time history of water level difference for simulations and experiments.

very similar.

Figure 7 shows a time series of the water level difference between the front and rear sides. The limitation of the water level difference in the experimental condition was 0.608 m and that in the calculation condition was 0.624 m. The mechanism of caisson movement under tsunami overflow is due to the water level difference producing a water force that pushes the caisson away. For the simulation, the friction coefficient was set to 0.6. Under the experimental conditions, the friction coefficient ranged from 0.59–0.57 [6]. Thus, if the friction coefficient were set to 0.59–0.57, the water level difference would be reduced by approximately 0.01 m. However, the calculated water level difference is larger than the experimental water level difference. Takahashi et al. [7] noted that the penetration flow in the rubble mound decreases the bearing capacity. Therefore, the reproducibility of the bearing capacity effect under this simulator should be determined in future work. Nevertheless, the result indicates that the system can reproduce the water force under tsunami overflow.

4. Application to Local Conditions

4.1. Target Area

Finally, this model was applied to a local tsunami disaster; specifically, breakwater damage due to the 2011 East Japan Earthquake Tsunami. **Fig. 8** shows the arrangement of breakwaters in Kamaishi bay, which consists of three breakwaters: the 990-m North Breakwater, the 670-m South Breakwater, and the 300-m submerged breakwater at the mouth of the bay. The crest height of all caissons is D.L. +6.0 m (T.P. +5.12 m) [6]. Caissons in the deep region have a rubble mound that extends from a depth of 60 m to 27 m. Almost half of the caissons were washed away by the tsunami.

4.2. Calculation Conditions

4.2.1. Calculation Domains

Figure 9 and **Table 1** show the calculation domains and specifications of the grid size, the number of cells, etc. The computational time was almost 3000 times longer than the physical time. The tsunami reached Kamaishi bay approximately 30 min after the earthquake; thus, it took more than 60 days for the computation. As a result, domain no.1 was made smaller to make the incident wave closer to the coastline and save computational time.

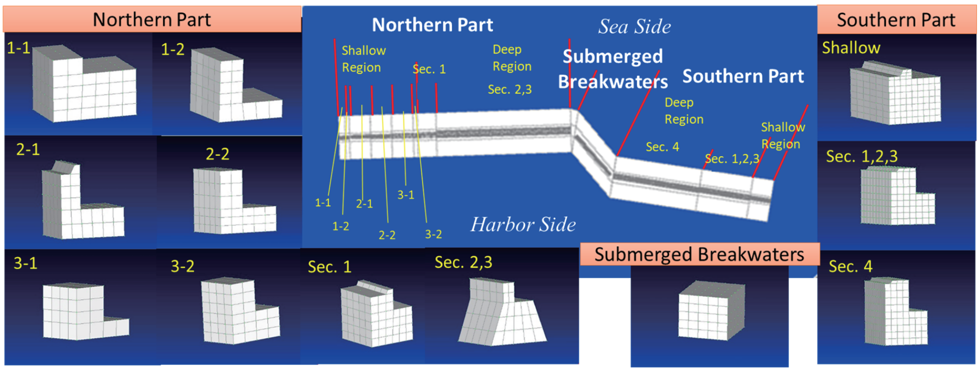

Fig. 8. Arrangement of the breakwaters at Kamaishi bay.

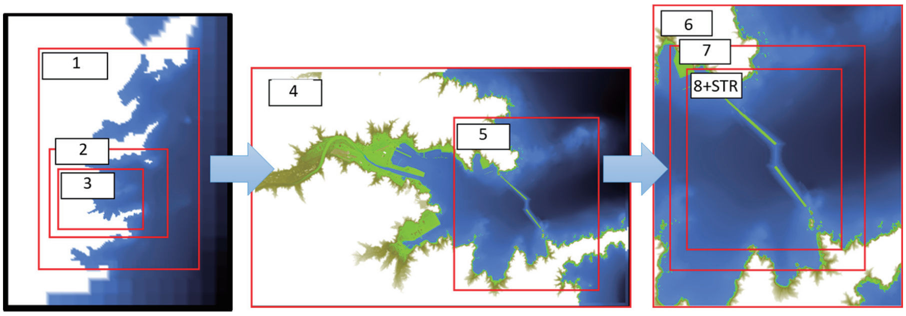

Fig. 9. Calculation domains.

Table 1. Computation conditions.

Domain Number	Solver	Grid size(m)	Number of Cells (X)	Number of Cells (Y)	Number of Cells (Z)	Number of CPUs
1	STOC-ML	200	108	141	1	1
2	STOC-ML	100	166	110	1	1
3	STOC-ML	50	240	150	1	1
4	STOC-ML	10	1100	690	1	1
5	STOC-ML	10	410	500	1	1
6	STOC-IC	10	330	400	1	1
7	CADMAS-MG	10	260	300	52	70
8	CADMAS-2FC	5	400	480	52	240
STR	STR	See Table 2				

4.2.2. Breakwater Conditions

Figure 8 also shows the cross-section of the caisson in each section. In order to minimize the influence on the stability of the caisson, the slit part in front of the caisson was eliminated in this calculation.

The property of the breakwaters and rubble mound are shown in **Table 2**. The static and dynamic friction coefficients were 0.6 and 0.4, respectively. In Section 3.1 in the northern shallow region, the friction enhancement mat was used; therefore, the friction coefficients were set as 0.8 and 0.6, respectively.

4.2.3. Incident Tsunami Wave Conditions

The time series of water level derived from the GPS wave gauge offshore of Kamaishi bay at the time of the Great East Japan Earthquake (39°15′31″E, 142°05′49″N) was incident from the east side boundary of the STOC calculation region of the outermost area (**Fig. 10**).

In addition, in order to save calculation time, data of the first 15 min were excluded (see **Fig. 11**). Furthermore, to ensure that the water level difference between the front and rear side of the breakwater coincides with the estimate of Arikawa et al. [7], the water level was set to 1.3 times greater than the observation.

4.3. Results

4.3.1. Tsunami Propagation

Figure 12 shows the tsunami propagation and the snapshot of domain 8 approximately 30 min after the shock. This indicates that the calculated propagation was stable.

Table 2. Property of breakwaters and rubble mound.

Type	Position	Depth	Section Name	Number of Caissons	Material	Young Modulus	Shear Modulus	Poisson ratio	Density [kg/m^3]
Breakwater	North	Shallow	1-1	2	Concrete without porosity	2.35×10^{10}	8.815×10^{7}	0.333	2010
			1-2	1					2040
			2-1	6					2010
			2-2	6					2020
			3-1	6					2030
			3-2	1					2000
		Deep	1	3					1980
			2, 3	19					1980
	Submerged			13					1900
	South	Shallow	1, 2, 3	3					2090
		Deep	1, 2, 3	7					2030
			4	12					1980
Mound					Foundation with porosity	2.00×10^{9}	7.692×10^{8}	0.333	1900

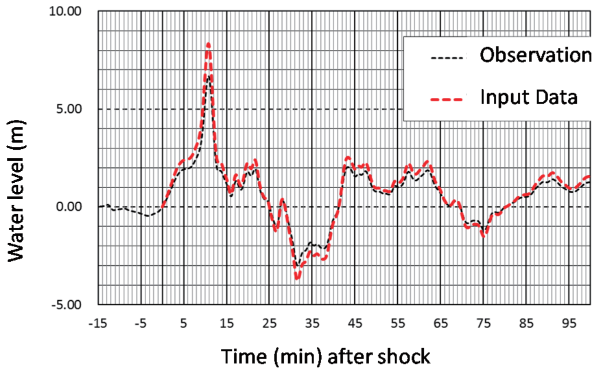

Fig. 10. Time history of GPS wave gauge derived wave profile for Kamaishi bay.

Fig. 11. Position of the wave boundary.

4.3.2. Movement of Submerged Breakwaters

Figure 13 shows the movement of the submerged breakwaters, which were washed away approximately 30 min after the earthquake. The velocity at the bay mouth was over 10 m/s, which is consistent with Arikawa et al. [8].

4.3.3. Movement of Northern Breakwaters

Figure 14 shows the movement of northern breakwaters. The breakwaters in Section 3.1 remained in place after the tsunami because of the friction enhancement mat.

The water level difference between the sea side and the harbor side is shown in **Fig. 15**, revealing that the caissons were moved when the water level difference was more than approximately 9.0 m at around 970 s. This result is in good agreement with the qualitative results of Arikawa et al. [6].

5. Summary

In this study, we developed a multiscale multiphysics integrated simulator for tsunami analysis (MMICST). This system connects five different programs to calculate not only tsunami propagation but also the destruction of structures from the epicenter to the coastal area. The validity of the model was verified through a comparison with physical experiments and actual damage by the 2011 East Japan Earthquake Tsunami. Both results indicated that the proposed system can reproduce structural damage due to tsunamis.

It is an important and urgent task to improve the calculation efficiency of this system to save computational time and make it applicable to a wide range of areas. From a physical point of view, analysis of the effects of scour and foundation destruction caused by landslides is a key task for future research.

Acknowledgements

This work was supported by Council for Science, Technology and Innovation (CSTI), Cross-ministerial Strategic Innovation Promotion Program (SIP), "Enhancement of societal resiliency against natural disasters" (Funding agency: JST). We thank Ministry of Land, Infrastructure, Transport and Tourism for the GPS data and the information about the cross section at Kamaishi port.

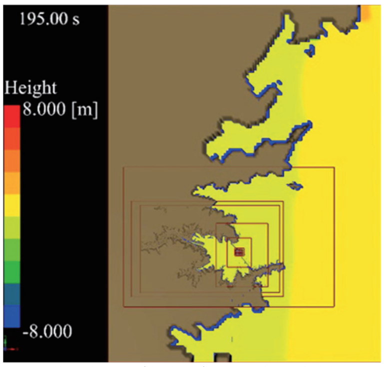

C.T.195 s (1095 s), L.T.15:04:33

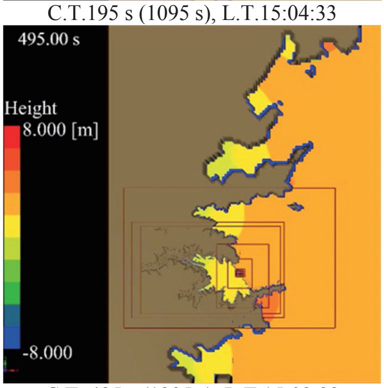

C.T. 495 s (1395 s), L.T.15:09:33

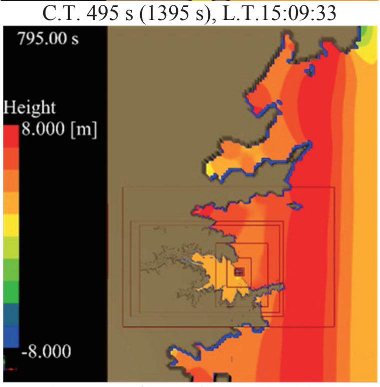

C.T. 795 s (1695 s), L.T. 15:14:33

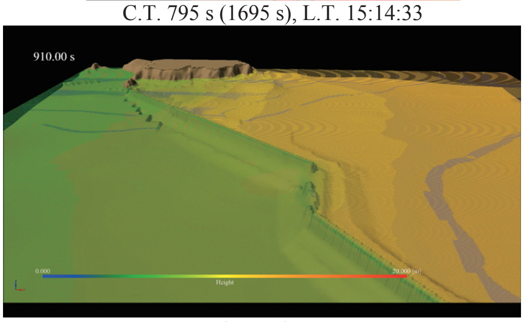

C.T. 905 s (1805 s), L.T. 15:16:23

Fig. 12. Tsunami propagation and snapshot of domain 8 (C.T.: computational time, L.T.: local time).

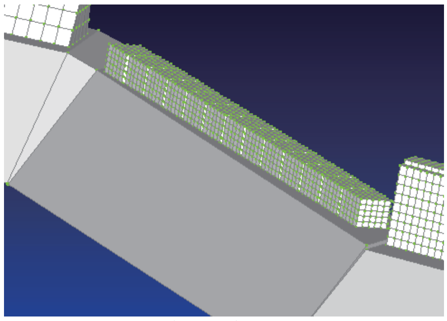

C.T.900 s (1800 s), L.T.15:16:18

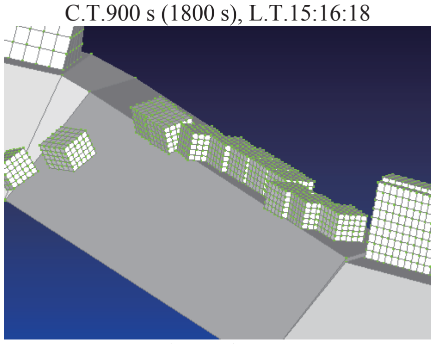

C.T. 910 s (1810 s), L.T.15:16:28

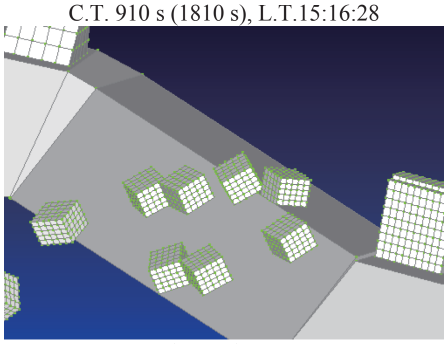

C.T. 920 s (1820 s), L.T. 15:16:38

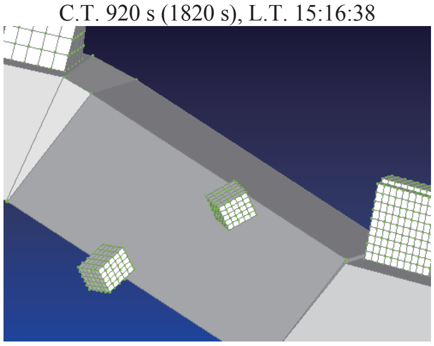

C.T. 930 s (1830 s), L.T. 15:16:48

Fig. 13. State of submerged breakwaters washed away by the tsunami (C.T.: computational time, L.T.: local time).

References:

[1] T. Tomita and T. Kakinuma, "Storm Surge and Tsunami Simulator in Oceans and Coastal Areas (STOC)," Report of the Port and Airport Research Institute, Vol.44, No.2, pp. 83-98, 2005 (in Japanese).

[2] T. Arikawa, F. Yamada, and M. Akiyama, "Study of Applicability of Tsunami Wave Force in a Three-Dimensional Numerical Wave Flume," Proc. of Coastal Engineering, Vol.52, pp. 46-50, 2005 (in Japanese).

[3] T. Arikawa, M. Akiyama, and Noboru Yamazaki, "Development of Solid-Gas-Liquid Coupling System by using CADMAS-SURF/3D," J. of Japan Society of Civil Engineers, Ser.B2 (Coastal Engineering), Vol.67, Issue 2, pp. I_21-I_25, 2011 (in Japanese).

[4] K. Hamaguchi, T. Arikawa, and K. Kitagawa, "Analysis of Deformation and Fracture of Seawall Joint using a Fluid-Structure Coupled System," J. of Japan Society of Civil Engineers, Ser.B2 (Coastal Engineering), Vol.67, Issue 2, pp. I_771-I_775, 2011 (in Japanese).

[5] T. Arikawa and T. Tomita, "Development of High Precision Tsunami Runup Calculation Method Based on a Hierarchical Simulation," J. Disaster Res., Vol.11, No.4, pp. 639-646, DOI: 10.20965/jdr.2016.p0639, 2016.

[6] T. Arikawa, M. Sato, K. Shimosako, I. Hasegawa, G.-S. Yeom, and T. Tomita, "Failure Mechanism of Kamaishi Breakwaters due to The Great East Japan Earthquake Tsunami," Coastal Engineering Proc., Vol.33, DOI: 10.9753/icce.v33.structures.16, 2012.

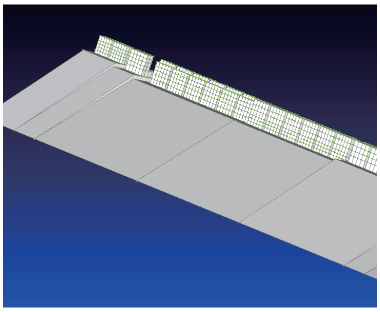

C.T. 970 s (1870 s), L.T. 15:17:28

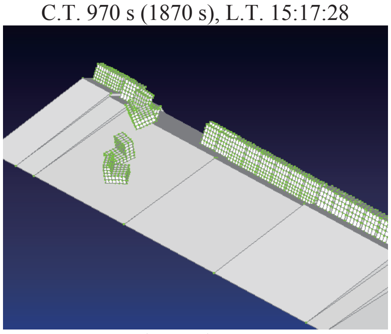

C.T. 985 s (1885 s), L.T. 15:17:43

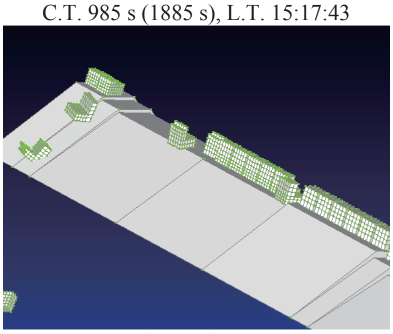

C.T. 995 s (1895 s), L.T.15:17:53

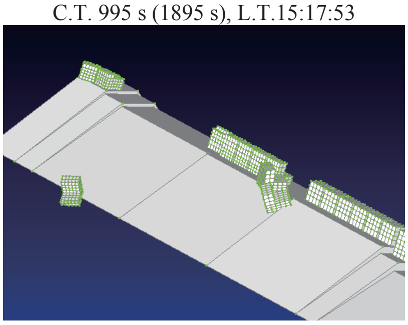

C.T. 1005 s (1905 s), L.T. 15:18:03

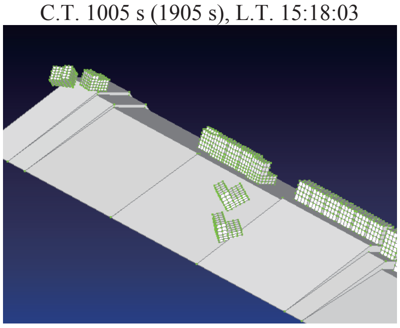

C.T. 1005 s (1905 s), L.T. 15:18:03

Fig. 14. State of northern breakwaters (C.T.: computational time, L.T.: local time).

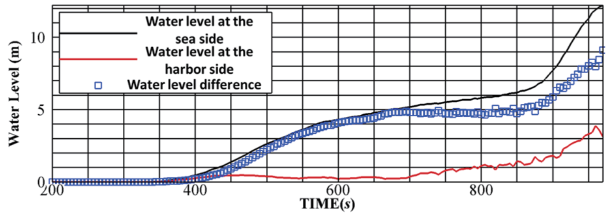

Fig. 15. Time history of calculated water level.

[7] H. Takahashi, S. Sassa, Y. Morikawa, and D. Takano, "Stability of Breakwater Foundation under Seepage Flow Caused by Tsunami," Report of the Port and Airport Research Institute, Vol.52, No.2, 2013 (in Japanese).

[8] T. Arikawa, M. Sato, K. Shimosako, T. Tomita, D. Tatsumi, G.-S. Yeom, and K. Takahashi, "Investigation Of The Failure Mechanism Of Kamaishi Breakwaters Due To Tsunami –Initial Report Focusing On Hydraulic Characteristics–," Technical Note of the Port and Airport Research Institute, No.1251, 2012 (in Japanese).

Name:
Taro Arikawa

Affiliation:
Professor, Department of Civil and Environmental Engineering, Faculty of Science and Engineering, Chuo University

Address:
1-13-27 Kasuga, Bunkyo-ku, Tokyo 112-8551, Japan

Brief Career:
2000- Joined Port and Airport Research Institute
2003- Senior Researcher, Maritime Structures Division
2015- Professor, Chuo University

Selected Publications:
• D. Wang, S. Shao, S. Li, Y. Shi, T. Arikawa, and H. Zhang, "3D ISPH erosion model for flow passing a vertical cylinder," J. of Fluids and Structures, Vol.78, pp. 374-399, 2018.
• H. G. Guler, C. Baykal, T. Arikawa, and A. C. Yalciner, "Numerical assessment of tsunami attack on a rubble mound breakwater using OpenFOAM®," Applied Ocean Research, Vol.72, pp. 76-91, 2018.
• T. Arikawa and T. Tomita, "Development of High Precision Tsunami Runup Calculation Method Based on a Hierarchical Simulation," J. Disaster Res., Vol.11, No.4, pp. 639-646, 2016.
• T. Arikawa and K. Shimosako, "Failure mechanism of breakwaters due to tsunami; a consideration to the resiliency," Proc. of 6th Civil Engineering Conf. in the Asian Region, No.301, 8pp., 2013.

Academic Societies & Scientific Organizations:
• Japan Society of Civil Engineers (JSCE)
• Architectural Institute of Japan (AIJ)
• Japan Association for Earthquake Engineering (JAEE)

Name:
Yu Chida

Affiliation:
Researcher, Tsunami and Storm Surge Research Group, Port and Airport Research Institute (PARI)

Address:
3-1-1 Nagase, Yokosuka, Kanagawa 239-0826 Japan

Brief Career:
2015 Joined Port and Airport Research Institute

Selected Publications:
• T. Tomita, T. Arikawa, T. Takagawa, K. Honda, Y. Chida, K. Sase, and R. Alejandro, "Results of Post-Field Survey on the Mw 8.3 Illapel Earthquake Tsunami in 2015," Coastal Engineering J., Vol.58, doi: 10.1142/S0578563416500030, 2016.

Academic Societies & Scientific Organizations:
• Japan Society of Civil Engineers (JSCE)

Name:
Katsumi Seki

Affiliation:
Associate Professor, Research and Development Initiative, Chuo University

Address:
1-13-27 Kasuga, Bunkyo-ku, Tokyo 112-8551, Japan

Brief Career:
2005- Research Associate, Chuo University
2008- Port and Airport Research Institute
2015- Associate Professor, Chuo University

Selected Publications:
• K. Seki, Y. Chida, T. Takagawa, T. Arikawa, and K. Shimosako, "Development Of Tsunami Inundation Evaluation Method Considering Damage Level Of Seawall," 36th Int. Conf. of Coastal Engineering, No.1319, 2018.

Academic Societies & Scientific Organizations:
• Japan Society of Civil Engineering (JSCE)
• Japan Society of Fluid Mechanics (JSFM)

Name:
Tomohiro Takagawa

Affiliation:
Group Head, Tsunami and Storm Surge Research Group, Port and Airport Research Institute (PARI)

Address:
3-1-1 Nagase, Yokosuka, Kanagawa 239-0826, Japan

Brief Career:
2007- Research Associate, The University of Tokyo
2011- Researcher, PARI
2015- Senior Researcher, PARI
2016- Group Head, PARI

Selected Publications:
• T. Takagawa, and T. Tomita, "Simultaneous inference of credible interval of inverted tsunami source and observation error by a hierarchical Bayes model," J. JSCE, Ser.B2, Coastal Engineering ! $Vol.70, pp. I_196-I_200, 2014.
• T. Takagawa and T. Tomita, "Effects of rupture processes in an inverse analysis of the tsunami source of the 2011 off the Pacific coast of Tohoku earthquake," Int. J. of Offshore and Polar Engineering, Vol.24, pp. 21-27, 2014.

Academic Societies & Scientific Organizations:
• Japan Society of Civil Engineers (JSCE)
• Seismological Society of Japan (SSJ)
• American Geophysical Union (AGU)

Name:
Kenichiro Shimosako

Affiliation:
Senior Director for Research, Port and Airport Research Institute (PARI)

Address:
3-1-1 Nagase, Yokosuka, Kanagawa 239-0826, Japan

Brief Career:
1986- Researcher, Port and Harbour Research Institute
1994- Senior Researcher, Port and Harbour Research Institute
1994-1995 Visiting Researcher, University of Bristol
2001- Head, Maritime Structures Division, Marine Environment and Engineering Department, PARI
2008- Director, Yokohama Research and Engineering Office for Port and Airport, Kanto Regional Development Bureau, Ministry of Land, Infrastructure, Transport and Tourism
2010- Director, Coastal and Ocean Engineering Research Field, PARI
2015- Senior Director for Research, PARI

Selected Publications:
• S. Maruyama, T. Takayama, K. Shimosako, A. Yahiro, K. Suzuki, T. Aota, M. Tanaka, A. Matsumoto, and M. Hanzawa, "Reducing performance of wave force and stability of wave-dissipating works against tsunami with soliton fission," J. JSCE, Ser.B2, Coastal Engineering, Vol.71, pp. I_265-I_270, 2015.

Academic Societies & Scientific Organizations:
• Japan Society of Civil Engineers (JSCE)
• Japan Society of Ocean Policy (JSOP)